Adaptive Multirate Moving Horizon Estimator for Real-Time Battery State and Parameter Estimation

Tushar Desai, Federico Oliva, Daniele Carnevale, and Riccardo M. G. Ferrari, *Senior Member, IEEE*

***Abstract*—Accurate and robust state of charge (SOC) estimation is vital for reliable and safe battery operations. However, the nonlinear and time-varying dependence of the model parameters on the battery states makes the problem challenging. To address this task, we propose a moving-horizon estimation (MHE)-based robust approach for joint state and parameter reconstruction. Due to its optimization-based nature, the computational burden of MHE is a crucial challenge. To overcome this, we introduce a real-time adaptive sampling method based on wavelet analysis. The resulting *adaptive multirate MHE* dynamically selects the best measurements for solving the estimation problem. Such an approach reduces the computational burden by focusing on the most informative data in the measurement buffer. Last, we implement a parallelized observer structure, combining both *multirate* and reduced-order MHEs to further lower the computational burden while maintaining estimation accuracy. The proposed methods are validated using a first-order equivalent circuit model on real battery datasets, under moderate operating conditions. The adaptive sampling framework extends naturally to higher-order models with appropriate recalibration for more demanding scenarios.**

***Index Terms*—Adaptive sampling, lithium-ion (Li-ion) battery, moving horizon estimation, parameter-varying systems, wavelet analysis.**

I. INTRODUCTION

LITHIUM-ION (Li-ion) batteries are seeing a surge in applications, with a rapidly growing electric vehicle (EV) market, as well as battery energy storage systems (BESSs). The high energy density and long cycle life make Li-ion batteries an attractive choice for such applications. However, to extend battery life and ensure safe operation, an effective battery management system (BMS) is essential [1].

Central to the BMS's functionality is the estimation of the state of charge (SOC), which represents the remaining battery capacity. Accurate SOC estimation is vital for range prediction in EVs and energy management in BESS, yet it cannot be measured directly. SOC must be inferred from current and voltage measurements, which is challenging because battery dynamics are nonlinear and vary with operating conditions. Estimation techniques fall into several categories. Open-loop methods, such as open-circuit voltage (OCV) lookup or Coulomb counting, are simple but either require long rest periods or suffer from cumulative sensor-noise errors [2]. Electrochemical (EC) models simulate detailed physicochemical processes but are too computationally heavy for real-time use [3]. Data-driven models, including machine learning approaches, learn nonlinear patterns from historical data but may not generalize beyond the training scenarios [4]. Finally, equivalent-circuit models (ECMs) approximate the battery as a network of resistors and capacitors; they offer a practical settlement between physical fidelity and computational efficiency, which makes them attractive for real-time BMS implementations [5].

The linear state dynamics and nonlinear output mapping of ECMs have led to the widespread use of nonlinear Kalman filter techniques for SOC estimation [6]. However, the nonlinear, time-varying dependence of ECM parameters on SOC, temperature, and battery health necessitates adaptive SOC estimation techniques to account for changes in battery dynamics [7]. To address this challenge, joint or dual Kalman filter-based approaches that simultaneously estimate both the state and parameters have been proposed [8]. Despite the widespread use of Kalman family algorithms, they have several limitations: their accuracy depends on the initialization of the states and, critically, on the tuning of the process and measurement noise covariance matrices [9]. Furthermore, Kalman filters cannot incorporate constraints on parameters and states, potentially leading to physically inconsistent estimates.

To overcome these limitations, alternative nonlinear observer techniques, such as moving horizon estimation (MHE) and high-gain observers, have been proposed [10]. The MHE, in particular, offers several advantages by utilizing an optimization framework over a receding horizon data window, improving resilience to modeling uncertainties and external disturbances, and producing smoother, more robust estimates compared to Kalman filters [11]. MHE has been applied to battery state and parameter estimation using both EC and ECMs [12], [13].

While MHE provides accurate and robust state and parameter estimation by optimizing over a receding time horizon, it comes with increased computational costs [14]. Recent research has explored integrating machine learning techniques with MHE to address these computational limitations [15], [16]. However, this hybrid approach inherits a critical limitation from ML-based methods: the models remain constrained by their training data, limiting their ability to generalize to new operating conditions.

The computational demands of MHE can limit its application to battery state estimation despite its superior constraint-handling capabilities. To mitigate this, we exploit the multitimescale nature of battery dynamics [17]. Our method optimizes both the observer horizon and measurement sampling rate by analyzing signal variability, a metric we developed in [18] and [19] to quantify information content in measurement sequences. We further implement adaptive sampling through real-time wavelet analysis. The primary contributions are given as follows.

1) *Adaptive Multirate MHE:* Measurement sampling rates are adjusted dynamically via wavelet decomposition, reducing computational requirements by concentrating estimation effort on information-rich portions of the measurement buffer. This approach enhances our signal richness criterion by incorporating a more robust frequency-domain analysis.
2) *Parallel Multirate MHE:* Two MHE instances operate concurrently: one targeting slow variables (SOC, parameters) and another tracking fast voltage transients. This dual-layer structure achieves real-time feasibility while maintaining estimation fidelity and enabling applications such as online model identification and fault detection.

Building on our prior work [20], which demonstrated fixed-rate downsampling MHE using simulated data with known ground truth,

Received 25 October 2025; accepted 24 December 2025. Date of publication 21 January 2026; date of current version 25 February 2026. This work was supported by Volvo AB (Sweden) and NWO (Netherlands) through TKI-HTSM under Grant 21.0056. Recommended by Associate Editor V. Adetola. *(Corresponding author: Tushar Desai.)*

Tushar Desai and Riccardo M. G. Ferrari are with Delft Center for Systems and Control, Delft University of Technology, 2628 Delft, The Netherlands (e-mail: t.k.desai@tudelft.nl; r.ferrari@tudelft.nl).

Federico Oliva is with the Department of Civil and Environmental Engineering, Technion Autonomous Systems Program, Technion–Israeli Institute of Technology, Haifa 3200003, Israel (e-mail: federicoo@campus.technion.ac.il).

Daniele Carnevale is with the Department of Civil Engineering and Computer Science, Tor Vergata University of Rome, 00133 Rome, Italy (e-mail: daniele.carnevale@uniroma2.it).

Digital Object Identifier 10.1109/TCST.2026.3650897

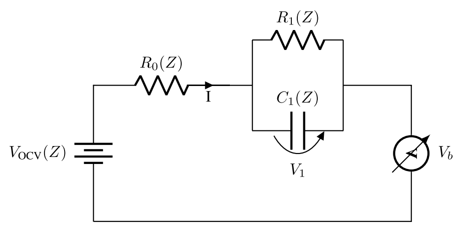

Fig. 1. First-order ECM of battery.

this study makes three key advances: 1) implementation of wavelet-driven adaptive sampling that responds to signal characteristics in real time; 2) integration with a parallel estimation framework for multitimescale dynamics; 3) systematic comparison with EKF under identical conditions; and 4) validation using experimental battery cycling data from the CALCE dataset.

The rest of this brief is organized as follows. Section II describes the SOC-dependent ECM model of the battery. Section III introduces the MHE framework, signal variability analysis, buffer length selection, wavelet analysis, and *adaptive multirate MHE*. Section IV details the validation dataset. Section V presents the results of the proposed MHE variants. Section VI concludes this brief and suggests future research directions.

II. Dynamic Modeling of Battery

The first-order ECM illustrated in Fig. 1 is selected for this study, balancing accuracy and computational efficiency for real-time BMS [21]. While higher-order models capture additional dynamics under extreme conditions, this model is adequate for moderate operation. The proposed methodology extends to higher-order structures by adjusting horizon lengths and sampling rates for the additional *RC* pairs. In the ECM, Z represents the SOC, V_{OCV} is the open-circuit voltage, R_0 is the ohmic resistance, and R_1 and C_1 are the polarization resistance and capacitance, respectively. The load current I is the exogenous input, V_b is the measured terminal voltage, and V_1 is the dynamic voltage across the *RC* pair. The ECM dynamics are described by the following equation:

$$Z_{k+1} = Z_k - \frac{\eta T_s I_k}{C_n} \tag{1a}$$

$$V_{1,k+1} = V_{1,k} e^{-\frac{T_s}{\tau_k}} + \left(1 - e^{-\frac{T_s}{\tau_k}}\right) R_1(Z_k) I_k \tag{1b}$$

$$V_{b,k} = V_{\mathrm{OCV}}(Z_k) - I_k R_0(Z_k) - V_{1,k} \tag{1c}$$

where $k \in \mathbb{Z}$ is the kth discrete time instant and T_s is the sampling time. C_n indicates the nominal battery capacity and can be measured through an offline capacity test, and η is the Coulombic efficiency. The time constant associated with the ECM is given by $\tau_k = R_1(Z_k)C_1(Z_k)$.

The nonlinear dependence of parameters on SOC can be approximated using higher-order polynomials [22], assuming that temperature remains constant during operation. Thus, the ECM parameters are modeled as functions of SOC

$$p(Z) = \sum_{i=0}^{P_p} \alpha_{p,i} \cdot Z^i, \quad \text{for } p \in \{V_{\mathrm{OCV}}, R_0, R_1, C_1\} \tag{2}$$

where $\alpha_{p,i}$ are the polynomial coefficients and P_p is the polynomial order for each parameter p. The order $P_{V_{\mathrm{OCV}}}$ is typically higher than that of other parameters, reflecting the highly nonlinear relationship between SOC and OCV. This SOC–OCV relationship can be characterized offline through low-current discharge or incremental capacity [23]. Although battery aging affects both the SOC–OCV relationship and nominal capacity over long periods, these parameters are assumed constant over the experimental timeframe due to the study's relatively short duration.

Indeed, it is necessary to update the remaining battery model parameters, i.e., (R_0, R_1, C_1), to address the model discrepancies arising from time-variant operating conditions. The resulting adaptive system consists of a nonlinear model incorporating both state dynamics and parameter evolution

$$\mathcal{P}: \begin{cases} \boldsymbol{\xi}_{k+1} = f(\boldsymbol{\xi}_k, u_k, \boldsymbol{\Theta}_k) + \mathbf{w}_{\xi,k} \\ \boldsymbol{\Theta}_{k+1} = g(\boldsymbol{\xi}_k, u_k, \boldsymbol{\Theta}_k) + \mathbf{w}_{\Theta,k} \\ y_k = h(\boldsymbol{\xi}_k, u_k, \boldsymbol{\Theta}_k) + v_k \end{cases} \tag{3}$$

where $u_k = I_k$ represents the load current and the measured output $y_k = V_{b,k}$ is the terminal voltage. $\boldsymbol{\xi}_k \in \mathbb{R}^2$ represents the system states with $\boldsymbol{\xi}_k = [Z_k, V_{1,k}]^\top$, and $\boldsymbol{\Theta}_k \in \mathbb{R}^{n_\Theta}$ denotes the parameter vector with $\boldsymbol{\Theta} = [\boldsymbol{\alpha}_{R_0}, \boldsymbol{\alpha}_{R_1}, \boldsymbol{\alpha}_{C_1}]^\top$.[1] Where required, we will also refer to the full state vector as $\boldsymbol{x}_k = [\boldsymbol{\xi}_k, \boldsymbol{\Theta}_k]^\top$. The polynomial coefficient vectors are defined as $\boldsymbol{\alpha}_p = [\alpha_{p,0}, \ldots, \alpha_{p,P_p}]^\top \in \mathbb{R}^{P_p+1}$ for $p \in R_0, R_1, C_1$, where $n_\Theta = \sum_{p \in R_0, R_1, C_1}(P_p + 1)$. The process noise terms $\mathbf{w}_{\xi,k} \in \mathbb{R}^2$ and $\mathbf{w}_{\Theta,k} \in \mathbb{R}^{n_\Theta}$ account for model uncertainties, while $v_k \in \mathbb{R}$ is the measurement noise.

First, we formulate the problem of joint state and parameter estimation as estimating the augmented state vector $\mathbf{x}_k = [\boldsymbol{\xi}_k, \boldsymbol{\Theta}_k]^\top$ from measurements y_k and inputs u_k.

III. Moving-Horizon Estimator

This section introduces moving-horizon estimations (MHEs) and their variants. We first introduce the *standard MHE* formulation. Building upon this, we then present a fixed-downsampling-based *single-rate MHE* to improve computational efficiency [18], [19]. Next, we use wavelet analysis to develop the adaptive-downsampling *multirate MHE*. Last, we introduce a *parallel MHE* structure to separate the estimation of fast and slow-evolving states.

A. Standard MHE

Consider the nonlinear system described in (3). The system is sampled with period T_s. We consider a downsampling of measurements such that samples are collected at time instants t_k with $t_k - t_{k-1} = N_{T_s} \cdot T_s$ where $N_{T_s} \in \mathbb{N}_{\geq 1}$ is the downsampling factor. The standard MHE considers $N_{T_s} = 1$.

To formulate the estimation problem, we first introduce the N-lifted system $H_k(\boldsymbol{\xi}, \boldsymbol{\Theta})$ concept, which represents a continuous system through a sequence of a finite number of discrete measurements [24]. Under the assumptions that: 1) the process noise $\mathbf{w}_{\xi,k}$ is negligible and 2) the parameter vector $\boldsymbol{\Theta}$ remains constant over the N-step horizon, the N-lifted system $H_k(\boldsymbol{\xi}, \boldsymbol{\Theta}) \in \mathbb{R}^{N\times 1}$ takes the form

$$\begin{bmatrix} h(\boldsymbol{\xi}_{k-N+1}, u_{k-N+1}, \boldsymbol{\Theta}) \\ h(f(\boldsymbol{\xi}_{k-N+1}, u_{k-N+1}, \boldsymbol{\Theta}), u_{k-N+2}, \boldsymbol{\Theta}) \\ h(f(f(\boldsymbol{\xi}_{k-N+1}, u_{k-N+1}, \boldsymbol{\Theta}), u_{k-N+2}, \boldsymbol{\Theta}), u_{k-N+3}, \boldsymbol{\Theta}) \\ \vdots \\ h(f^{[N-1]}(\boldsymbol{\xi}_{k-N+1}, u_{k-N+1:k-1}, \boldsymbol{\Theta}), u_k, \boldsymbol{\Theta}) \end{bmatrix}. \tag{4}$$

The system is also assumed to be $(N+1)$-step observable as per [25]. We recall here the definition for the sake of completeness.

Definition 1 (N-Step Observability): Consider system $\mathcal{P}$ with dynamics from (3) and its N-lifting accordingly to (4). System $\mathcal{P}$ is assumed to be N-step observable if there exist constants $r_\delta, \delta > 0$ such that

$$\sum_{i=k-N}^{k} \left|\left| h(\boldsymbol{\xi}_i^{(1)}, u_i, \boldsymbol{\Theta}_i) - h(\boldsymbol{\xi}_i^{(2)}, u_i, \boldsymbol{\Theta}_i) \right|\right| \geq \delta^2 \left|\left| \boldsymbol{\xi}_{k-N}^{(1)} - \boldsymbol{\xi}_{k-N}^{(2)} \right|\right| \tag{5}$$

for each $k \geq N$ and any trajectories $\boldsymbol{\xi}^{(j)}$ satisfying $||\boldsymbol{\xi}_{k-N}^{(j)} - \boldsymbol{\xi}_{k-N}^*|| < r_\delta$, $j = 1, 2$.

[1] A small notation remark: bold lowercase letters refer to vectors.

The N-step observability relates to system detectability and requires distinguishable state trajectories as shown in Definition 1. Satisfaction of inequality (5) depends on sufficient persistent excitation over horizon N. Rich input–output variations (e.g., charge–discharge transitions or dynamic current profiles) ensure unique identifiability of $\boldsymbol{\xi}$ and $\boldsymbol{\Theta}$. Under persistently low excitation (constant current or idle conditions), the system may lose observability, necessitating an extended horizon N or improved input excitation.

An MHE consists of a nonlinear observer solving the following optimization problem in the estimated variables $(\hat{\boldsymbol{\xi}}_{k-N+1}, \hat{\boldsymbol{\Theta}}_{k-N+1})$:

$$\min_{\substack{\hat{\boldsymbol{\xi}}_{k-N+1}\\ \hat{\boldsymbol{\Theta}}_{k-N+1}}} J = W_1 \underbrace{\left|\left|Y_k - \hat{H}_k\right|\right|}_{\textbf{output mismatch}} + \underbrace{W_2 \left|\left|\hat{\boldsymbol{\xi}}_{k-N+1} - \hat{\boldsymbol{\xi}}^0\right|\right| + W_3 \left|\left|\hat{\boldsymbol{\Theta}}_{k-N+1} - \hat{\boldsymbol{\Theta}}^0\right|\right|}_{\textbf{arrival cost}} \quad \text{s.t.} \quad (3) \tag{6}$$

where W_i are scaling factors designed to normalize all the terms in the cost function J and $(\hat{\boldsymbol{\xi}}^0, \hat{\boldsymbol{\Theta}}^0)$ are the estimated values at the beginning of the optimization. Moreover, the measurement buffer $Y_k = [y_{k-N+1}, \ldots, y_k]^T \in \mathbb{R}^N$ contains N sequential outputs starting from t_{k-N+1}. Since this formulation optimizes only the initial estimates $(\hat{\boldsymbol{\xi}}_{k-N+1}, \hat{\boldsymbol{\Theta}}_{k-N+1})$, with subsequent trajectory determined through forward integration, it represents a single-shooting MHE approach [26]. In this brief, to solve the optimization problem in (6), we considered the MATLAB built-in simplex-like **fminsearch** optimization algorithm, with a fixed number of iterations $K = 1$. The number of iterations is usually limited to reduce the computational time of the estimation process even though this implies a suboptimal observer. Local and practical stability results have been introduced in [25], stating the necessity of the arrival cost term in the minimization, highlighted in (6).

B. Fixed-Downsampling MHE

The main issue with MHEs is the computational cost, which increases with the buffer length due to the evaluation of $H_k(\hat{\boldsymbol{\xi}}_{k-N+1}, \hat{\boldsymbol{\Theta}}_{k-N+1})$ in (6), as the plant dynamics in (3) are integrated for a longer interval.[2] We recall that $N \geq n$, where n is the model order, is a necessary condition on the buffer length to obtain a local convergence of the estimation [26], while [27] proves $N \geq 2n + 1$ to be a sufficient condition for the estimation error convergence. Therefore, computational cost increases with the model dimension. To increase MHE efficiency, we exploit the *signal variability* index δ_y from [19], which quantifies measurement informativeness relative to the buffer Y_k

$$\delta_y\left(k, q, N_{T_s}\right) = \sum_{i=1}^{N-1} \left\| y_{k-iN_{T_s}} - y_{k-(i+1)N_{T_s}} \right\| + \left\| y_{k+qT_s} - y_k \right\| \tag{7}$$

with $q \in [0, N_{T_s} - 1]$. Even though δ_y considers the measurements already present in the buffer, it is evaluated at each y_k. The index δ_y quantifies signal variability over the MHE horizon and can be used to tune N_{T_s} for robust estimation [20]. Following the Shannon–Nyquist theorem, N_{T_s} must ensure sufficient samples to reconstruct the dynamics of interest. Given an estimated bandwidth $\overline{B_{\mathrm{Hz}}}$ (e.g., via `tfest` in MATLAB), the downsampling factor is selected to satisfy

$$\overline{N_{T_s}} = \left\lceil \frac{1}{2 \cdot \overline{B_{\mathrm{Hz}}} \cdot T_s} \right\rceil. \tag{8}$$

[2]LTI systems' integration can be significantly sped up through closed-form solutions of the ODEs.

C. Adaptive Multirate MHE

This section introduces our first solution to reduce the computational burden of the *standard MHE* observers, which we will call the *adaptive multirate MHE*. This solution aims to properly select the measurement downsampling factor N_{T_s}, together with the spectral analysis of our system, to improve the *standard MHE* performance. Specifically, the proposed method selects the best measurements for estimation by adaptively changing the downsampling factor N_{T_s}.

Wavelet analysis is particularly suitable for battery state estimation due to the multitimescale nature of battery dynamics, and voltage exhibits fast transients during current switching and slow variations during steady-state operation [17]. Unlike the signal richness metric δ_y from our previous work [18], which depends on the already-downsampled buffer Y_k, wavelets enable localized time–frequency analysis of the raw measurement buffer independently. This decoupling eliminates dependence on previous sample selections and improves robustness to measurement noise and rapidly vanishing frequency peaks while enabling adaptive sampling: dense during transients and sparse during steady states.

1) Wavelets: The signal richness δ_y from (7) indicates how well buffer Y_k describes system evolution but depends directly on the downsampled measurements. We instead employ wavelets for localized time–frequency analysis of raw measurements. The continuous wavelet transform (CWT) is defined as [28]

$$W_\Psi f(b, a) = \int_{-\infty}^{+\infty} f(t)\, \Psi_{b,a}(t)\, dt \tag{9a}$$

$$\Psi_{b,a}(t) = \frac{1}{\sqrt{a}} \Psi\left(\frac{t-b}{a}\right) \quad \text{with } a > 0 \tag{9b}$$

where the parameters (a, b) are called *dilation* and *translation*. The choice of the mapping Ψ depends on the wavelet design and plays a key role in the transform [29].

2) Adaptive Sampling: We now present the *adaptive multirate MHE*, exploiting the CWT to autonomously select the downsampling factor N_{T_s}. At every time instant t_k, the main idea of the *adaptive multirate MHE* consists of applying a CWT to the last N_Ψ measurements and extracting the main frequency characterizing the output signal within that time window. For the CWT, we process the output of the `cwt` method from the `MATLAB` wavelet toolbox, returning a vector of frequencies for each element in the time-series signal. It is then straightforward to extract the maximum frequency identified in the provided time window

$$F_{\max} = \max \mathtt{cwt}\left(Y_\Psi, \Psi\right) \tag{10}$$

where Y_Ψ is the N_Ψ-long output buffer on which the CWT is computed and Ψ is the window function. Considering $F_{\max}$ as the measurement signal bandwidth estimate, from (8) and (10), we compute our downsampling as follows:

$$N_{T_s,\Psi} = \max\left(N_{T_s,\min}, \left\lceil \frac{1}{T_s \cdot 2 \cdot F_{\max}} \right\rceil\right) \tag{11a}$$

where T_s is the sampling time and $N_{T_s,\min} \in \mathbb{N}_{\geq 1}$ is the minimum admissible downsampling (usually $N_{T_s,\min} = 1$).

In the *adaptive multirate MHE*, at every time instant, the CWT defines a downsampling factor $N_{T_s,\Psi}$ depending on the current time–frequency analysis. We remark that $N_{T_s,\Psi}$ changes at every new measurement. This approach increases robustness against measurement noise and rapidly vanishing frequency peaks.

D. Parallel Multirate MHE

As previously mentioned, the main drawback of the *standard MHE* and *adaptive multirate MHE* lies in the fact that the computational effort increases with N_{T_s}. This computational challenge can be addressed by leveraging the inherent time-scale separation in battery dynamics. Since the temperature is held constant and SOC dependence is explicitly modeled through polynomials in (2), parameter variations are mainly attributed to aging phenomena, which evolve at

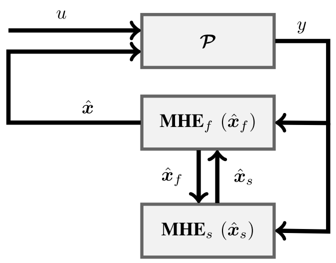

Fig. 2. Parallel MHE scheme.

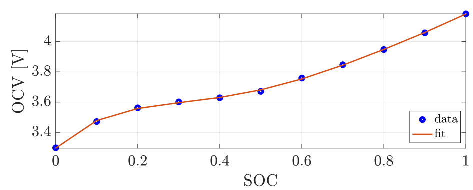

Fig. 3. SOC–OCV relationship at 25 °C, with fifth-order polynomial fit.

a significantly lower rate compared to voltage dynamics. Exploiting this inherent time-scale separation, we define the augmented state vector in terms of fast and slow subspaces

$$x_k = \left[x_k^f, \boldsymbol{x}_k^s\right]^\top, \quad \text{where} \quad x_k^f = V_{1,k}, \quad \boldsymbol{x}_k^s = [Z_k, \boldsymbol{\Theta}_k]^\top. \tag{12}$$

This state separation motivates two parallel estimators, each operating with distinct buffer lengths and sampling rates.

1) *MHE$_s$*: Operates with buffer length N^s and downsampling factor $N_{T_s}^s$ for estimation of $\boldsymbol{x}_k^s$.
2) *MHE$_f$*: Operates with buffer length N^f and downsampling factor $N_{T_s}^f$ for estimation of x_k^f.

The corresponding optimization problems are formulated as follows:

$$\begin{aligned} \text{MHE}_f: \min_{\hat{x}^f_{k-N_f+1}} \; & W_1^f \left\| \mathbf{Y}_k^f - \hat{\mathbf{H}}_k^f \right\| + W_2^f \left\| \hat{\boldsymbol{x}}^f_{k-N_f+1} - \hat{\boldsymbol{x}}^{f,0} \right\| \\ \text{MHE}_s: \min_{\hat{\boldsymbol{x}}^s_{k-N_s+1}} \; & W_1^s \left\| \mathbf{Y}_k - \hat{\mathbf{H}}_k^s \right\| + W_2^s \left\| \hat{\boldsymbol{x}}^s_{k-N_s+1} - \hat{\boldsymbol{x}}^{s,0} \right\| \end{aligned} \tag{13}$$

where $\hat{\mathbf{H}}_k^f$ and $\hat{\mathbf{H}}_k^s$ denote the N-lifted system outputs corresponding to fast and slow dynamics, respectively. The two estimators are interconnected via state feedback: MHE$_f$ updates its slow states using $\hat{\boldsymbol{x}}_k^s$ from MHE$_s$, while MHE$_s$ utilizes the trajectory of $\hat{\boldsymbol{x}}_k^f$ from MHE$_f$ over its horizon. The observer structure is shown in Fig. 2, where $\mathcal{P}$ represents the plant dynamics in (3).

IV. Data

We validate our approach using an open-source battery dataset from the Center for Advanced Life Cycle Engineering (CALCE) at the University of Maryland [30]. The dataset features a cylindrical INR 18650-20R LiNiMnCo/Graphite cell with a nominal capacity of 2 Ah, denoted as C_n. The battery undergoes low-current and incremental-current OCV tests at three different temperatures. For this study, we selected the incremental current-based OCV test at 25 °C, as it has been shown to provide more accurate SOC estimation results compared to the low-current test [23]. The measured SOC–OCV data are fit with a fifth-order polynomial. Fig. 3 illustrates the SOC–OCV curve with a polynomial fit. The fit polynomial can be expressed as follows:

$$\begin{aligned} V_{\text{OCV}}(Z) = 3.2765 + 2.7349Z - 9.7545Z^2 \\ + 17.7884Z^3 - 14.0073Z^4 + 4.1434Z^5. \end{aligned} \tag{14}$$

To validate the model, we use a dynamic current discharge based on the dynamic stress test (DST) driving cycle, as illustrated in Fig. 4.

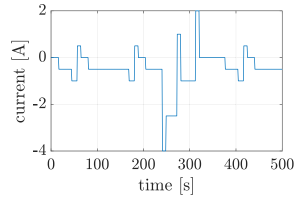

Fig. 4. Current profiles for the DST driving cycle.

The protocol involves discharging the cell from an initial SOC of 80% to the end of discharge (EOD), with data acquired at a sampling frequency of 1 Hz.

V. Results and Discussion

This section evaluates the joint state–parameter estimator from Section II via the standard MHE and its variants. We first compare the *standard MHE* with a joint EKF using root mean square error (RMSE) and then assess the MHE variants.

A. Standard MHE and EKF Comparison

The *standard MHE* approach, as defined in (6), is applied to the joint state and parameter estimation problem. In this formulation, we estimate the variables $\boldsymbol{\xi} = (Z, V_1)$ and parameters $\boldsymbol{\Theta} = (\alpha_{R_0,0-3}, \alpha_{R_1,0-3}, \alpha_{C_1,0-3})$. Following the guideline from [27], we set up a buffer with $(N = 30, N_{T_s} = 1)$, where $N \geq 2(\dim(\boldsymbol{\xi}) + \dim(\boldsymbol{\Theta})) + 1 = 29$.

As pointed out by [13], the estimation of V_b is prone to instabilities. By inspecting (1), it is evident that such instabilities occur in two forms: numerical instabilities, as $(R_0(Z), R_1(Z))$ approach zero values, and model instabilities when these parameters become negative. As demonstrated in [20], the state estimation can diverge when the optimization process results in negative values for R_1. We first implement a soft constraint to address this limitation by modifying the cost function in (6). This modification penalizes Θ values resulting in $(R_0(Z), R_1(Z))$ approaching zero

$$\begin{aligned} \min_{\substack{\hat{\xi}_{k-N+1} \\ \hat{\boldsymbol{\Theta}}_{k-N+1}}} \; J = \mathrm{W}_1 \left\| Y_k - \hat{H}_k \right\| + W_2 \left\| \hat{\boldsymbol{\xi}}_{k-N+1} - \hat{\boldsymbol{\xi}}^0 \right\| \\ + W_3 \left\| \hat{\boldsymbol{\Theta}}_{k-N+1} - \hat{\boldsymbol{\Theta}}^0 \right\| + c_{R_0}\left(\hat{\boldsymbol{\Theta}}_{k-N+1}\right) \\ + c_{R_1}\left(\hat{\boldsymbol{\Theta}}_{k-N+1}\right) \end{aligned} \tag{15}$$

where c_R is defined by $c_R = 0$ if $R \geq 0$ and $c_R = M$ otherwise, with M chosen sufficiently large, for example, $\bar{M} = 10^5$.

Note that such constraints cannot be directly incorporated into the EKF framework due to its formulation [11]. While MHE allows for constraint handling through cost function modification, EKF relies on covariance matrix tuning. During our extensive grid-based parameter search for covariance matrices, we observed that certain combinations of covariance values led to a complete divergence of the EKF. Through this systematic search, we determined the optimal EKF parameters as $\mathbf{P}_0 = \text{diag}(10^{-2}, 10^{-2}, 10^{-6}, \ldots, 10^{-6})$, $\mathbf{Q} = \text{diag}(10^{-4}, 10^{-3}, 10^{-6}, \ldots, 10^{-6})$, and $R = 10^{-6}$. Here, the first two scalars always refer to the (Z, V_1) estimation while the remaining to the model parameters. This sensitivity to covariance matrix tuning aligns with previous findings [9], [31], whereas MHE's single-shooting structure demonstrates more robust behavior.

The comparison between MHE and EKF for joint state–parameter estimation was performed with initial SOC values of $\hat{Z}_0 = 0.4$ and 0.6, as shown in Fig. 5. The results indicate that MHE achieves faster convergence than EKF and maintains better tracking throughout the entire test duration. The initial short delay observed in MHE's estimation is due to the requirement of filling the moving horizon buffer ($N = 30$). The overall estimation error, quantified by RMSE and detailed in Table I, shows how the MHE consistently estimates

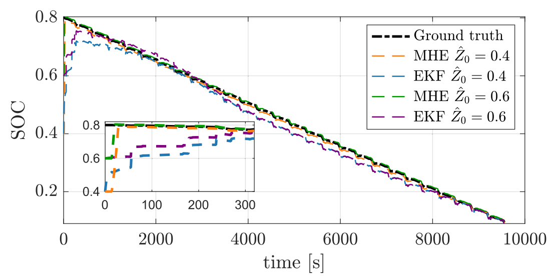

Fig. 5. SOC estimation comparison using *standard MHE* ($N = 30$) and EKF, with initial values $\hat{Z}_0 = 0.4$ and $\hat{Z}_0 = 0.6$.

TABLE I

SOC Estimation Error and Mean Computational Time per Iteration for EKF and *Standard MHE* ($N = 30$)

$\hat{Z}_0$	SOC (RMSE)		Mean Time (s)	
	MHE	**EKF**	**MHE**	**EKF**
0.4	0.0075	0.0390	0.1247 s	2.215×10^{-5} s
0.6	0.0041	0.0290	0.1375 s	2.190×10^{-5} s

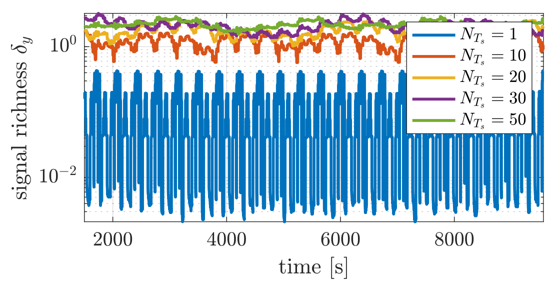

Fig. 6. Signal richness δ_y, with varying N_{T_s}. Values in the logarithmic scale.

SOC with significantly lower errors than the EKF, regardless of the initial SOC value. Overall, MHE consistently achieves faster convergence and lower estimation errors than EKF.

However, this improved estimation accuracy comes at a computational cost. As from Table I, MHE requires 0.125–0.138 s per iteration,[3] significantly higher than EKF's 2.1–2.3 $\times$ 10^{-5} s. We now discuss the MHE variants' performance in reducing such computational costs.

B. Fixed-Downsampling MHE

We compare estimator performance for different downsampling factors N_{T_s}. Because the terminal voltage V_b varies slowly over roughly 1000 s relative to the sampling period T_s, choosing a small N_{T_s} yields a measurement buffer Y_k with little variation in Z. This small variability makes it difficult to identify higher-order polynomial parameters $(\alpha_{R_0,0-3}, \alpha_{R_1,0-3}, \alpha_{C_1,0-3})$, as Y_k is insensitive to them over such a narrow range of Z values [13]. We, therefore, examine N_{T_s} values that maximize signal variability to improve estimation accuracy.

Indeed, as discussed in [18], selecting the downsampling factor N_{T_s} that best improves the estimation performance coincides with choosing the one maximizing δ_y. Fig. 6 plots δ_y for the DST cycle over the entire trajectory using (7) and various N_{T_s} values (with $N = 30$).[4] Although δ_y generally increases with N_{T_s}, the response indicates cycle-dependent fluctuations. The averaged curve (see Fig. 7) has a distinct knee at $N_{T_s} = 10$, so this value is used in subsequent estimations.

[3] All computations were performed on a Quad-Core Intel Core i7 processor.

[4] The period considered begins after the measurement buffers are filled.

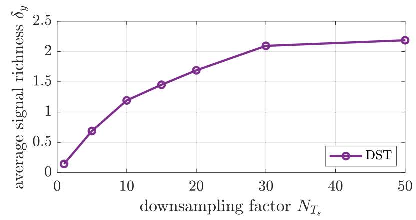

Fig. 7. N_{T_s} knee-like behavior. Each datapoint averages all the δ_y's computed.

TABLE II

Comparison of SOC Estimation Error and Computational Performance for $N_{T_s} = 1$ and $N_{T_s} = 10$

N_{T_s}	**RMSE**	$\boldsymbol{\mu}$ (mean)	$\boldsymbol{\sigma}$ (std. dev.)	**Total Time (s)**	**Opt. Count**
1	0.0075	0.1247 s	0.0291 s	1268 s	9551
10	0.0079	0.1100 s	0.3759 s	1180 s	942

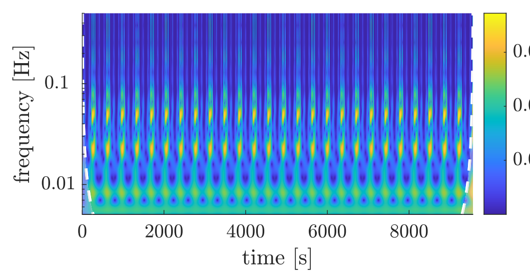

Fig. 8. CWT scalogram of battery voltage for the DST cycle.

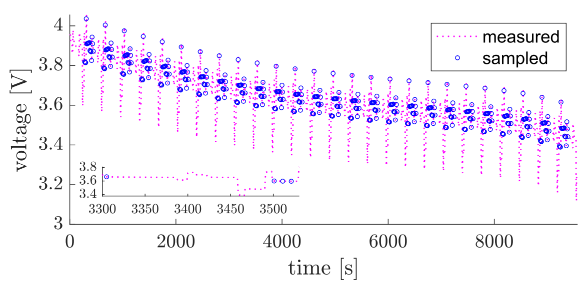

Fig. 9. Adaptive downsampling using the wavelet analysis.

The MHE with $N_{T_s} = 10$ shows SOC estimation RMSE values ranging from 0.0078 to 0.0107, as reported in Table II. This performance is comparable to the *standard MHE* with $N_{T_s} = 1$. Importantly, the total number of optimization problems decreased from approximately 9600 to about 950, reducing the computational load by a factor of 10. The mean computational time per iteration decreased with increased standard deviation due to more model integrations per optimization step. This initial analysis with $N_{T_s} = 10$ indicates that fixed downsampling can reduce the computational costs while maintaining estimation accuracy. However, as illustrated in Fig. 6, the signal richness δ_y varies throughout the driving cycle. This variability suggests that a fixed downsampling factor may still not consistently capture the most informative measurements for the estimation process. To address this issue, we further explore the real-time adaptive multirate MHE.

C. Adaptive Multirate MHE

We present the results of wavelet-based real-time adaptive MHE. The CWT computed over the voltage measurements of the current profile is presented in Fig. 8 and provides insights into the frequency

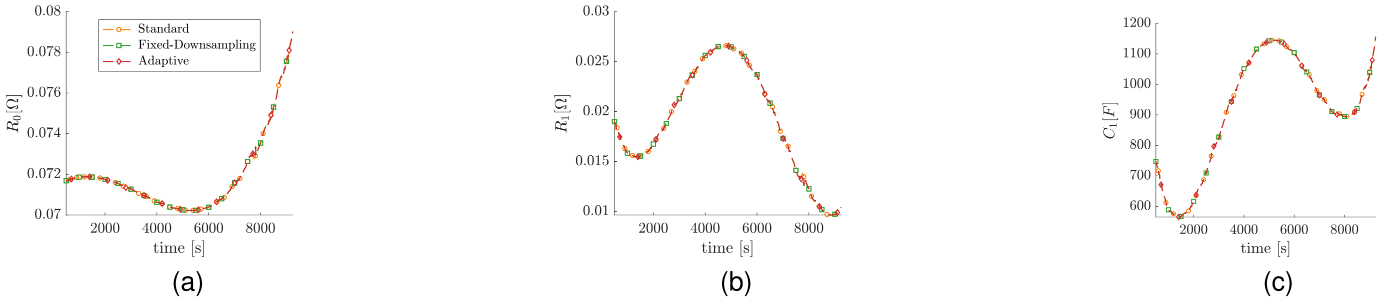

Fig. 10. Estimated parameters with *standard*, *fixed-downsampling*, and *adaptive multirate* MHEs. (a) R_0. (b) R_1. (c) C_1.

TABLE III

COMPARISON OF SOC ESTIMATION ERROR AND COMPUTATIONAL PERFORMANCE FOR FIXED AND ADAPTIVE MULTIRATE MHE

Method	RMSE	μ(mean)	σ(std. dev.)	Total Time (s)	Opt. Count
Fixed	0.0079	0.1100 s	0.3579 s	1180 s	942
Adaptive	0.0075	0.1055 s	0.4833 s	1012 s	428

characteristics of the signals. The DST profile has a dominant carrier frequency in the range of 0.02–0.04 Hz.

At each instant t_k, we consider $N_\Psi = 20$ last measurements, denoted as Y_Ψ, from the $N = 30$ measurement buffer. The resultant $F_{\max}$ obtained through CWT analysis is upscaled by $F_{nyq} = 10$ to satisfy the Nyquist criteria, as mentioned in (11). However, as our emphasis here is to capture the slower dynamics, we further set the $N_{T_s,\min} = 10$ in (11) according to the analysis we did in the Section V-B. This results in a minimum buffer length of $N_{T_s,\min} \cdot N_\Psi = 200$ s, on which wavelet analysis is computed. Adaptive measurements selected for estimation during the runtime are presented in Fig. 9.

The comparison of SOC estimation error and computational performance among fixed-downsampling MHE ($N_{T_s} = 10$) and adaptive multirate MHE with ($N_{T_s,\min} = 10$) is shown in Table III. The comparative analysis shows that SOC estimation accuracy remains comparable between fixed-down sampling and adaptive multirate MHE. However, the adaptive approach significantly reduces computational load, noticeable in the optimization count, which decreased by 54% for DST cycle. Despite the additional wavelet analysis overhead in adaptive MHE, the total simulation time is still reduced for adaptive ones.

To further illustrate the performance of the adaptive multirate MHE, Fig. 10 compares the estimated parameters R_0, R_1, and C_1 across *standard*, *fixed-downsampling*, and *adaptive multirate* MHEs. All three methods show similar trends in the estimated parameters, indicating consistency across the approaches. In earlier work [20], these estimations were validated against known ground truth parameters for accuracy. However, in this study, no known ground truth is available.

Back to the computational performance, increasing $N_{T_s,\min}$ in *adaptive multirate* can further reduce the computational burden. However, relying on a single optimization with high N_{T_s} to track both fast and slow dynamics can lead to poor estimation of the fast voltage dynamics. To address this problem, the *parallel MHE* approach leverages separate MHE instances operating at different timescales to track both the fast voltage dynamics and the slower SOC and parameter variations.

D. Parallel MHE

The *parallel* MHE framework involves two MHE instances operating concurrently, as shown in Fig. 2.

1) MHE_s: *Adaptive multirate* MHE with $N^s = 30$ and $N^s_{T_s}$ variable with $N^s_{T_s,\min} = 30$. The optimized variables are $\xi_s = (Z_s, V_{1,s})$ and $\mathbf{\Theta}_s = (\alpha_{R_0,0-3}, \alpha_{R_1,0-3}, \alpha_{C_1,0-3})$.

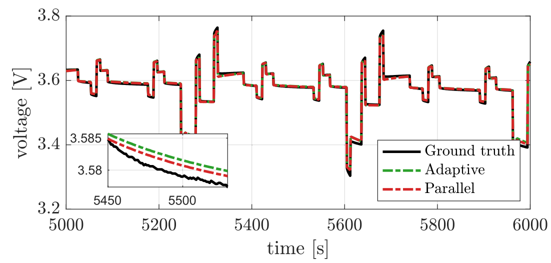

Fig. 11. Voltage's comparison with *adaptive multirate* and *parallel* MHEs.

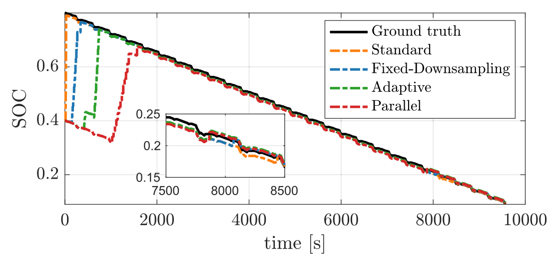

Fig. 12. Comparison of SOC estimation using multiple MHE variants.

TABLE IV

COMPUTATIONAL TIME COMPARISON FOR FAST AND SLOW MHE VARIANTS PROCESSING 9500 S (2.6 H) OF BATTERY DATA AT 1 HZ

Algorithm	μ (mean)	σ (std. dev.)	Total time	Opt. count
MHE_s	0.1037 s	0.5851 s	991.45 s	283
MHE_f	0.0080 s	0.0341 s	76.30 s	957

2) MHE_f: *Adaptive multirate* MHE with $N^f = 5$ and $N^f_{T_s}$ variable with $N^f_{T_s,\min} = 1$. The optimized variables are $\xi_f = V_{1,f}$. Moreover, $\mathbf{\Theta}_f$ is updated to $\mathbf{\Theta}_s$ every $N^s_{T_s}$ s.

The MHE_f achieves higher voltage estimation accuracy compared to the single-instance MHE implementation, as shown in Fig. 11. This improvement comes from its shorter horizon length and increased optimization frequency for the $V_{1,f}$ state. The SOC estimation accuracy of MHE_s remains consistent with other MHE variants (see Fig. 12) while reducing the optimizations through an increased $N_{T_s,\min}$ value.

The computational analysis in Table IV shows that MHE_f has a mean iteration time of 0.0080 s. The proposed framework's parallel architecture leverages the battery system's inherent multitimescale nature. By combining the 0.0080-s voltage tracking iterations of MHE_f with the reduced number of optimizations and longer horizon length for SOC and parameter estimation in MHE_s, the *parallel MHE* approach provides a computationally efficient solution suitable for real-time implementation.

VI. Conclusion

In this work, we evaluate a MHE for estimating the SOC and model parameters of Li-ion batteries. We find that estimation performance depends on the window buffer length and the sampling time. Using a *signal variability index*, we develop a procedure to select the MHE window size and (down) sampling factor (N_{T_s}) to improve estimation accuracy. We introduce an *adaptive multirate MHE* algorithm that dynamically adjusts the sampling rate using wavelet-based signal analysis. This algorithm captures dynamics occurring at different time scales by focusing computational efforts on the most informative data. We also propose a *parallel MHE* architecture that estimates slow and fast system dynamics concurrently through real-time adaptive sampling. This maintains estimation accuracy while reducing the computational load to enable real-time implementation. We validate our methods using multiple current profiles from real battery datasets. Future work will extend the framework to higher-order equivalent circuit models for more demanding operating conditions and will incorporate thermal and aging effects by reconstructing the SOC–OCV mapping and estimating battery capacity within the parallel MHE framework.

References

[1] S. Nyamathulla and C. Dhanamjayulu, "A review of battery energy storage systems and advanced battery management system for different applications: Challenges and recommendations," *J. Energy Storage*, vol. 86, May 2024, Art. no. 111179.

[2] K. S. Ng, C.-S. Moo, Y.-P. Chen, and Y.-C. Hsieh, "Enhanced Coulomb counting method for estimating state-of-charge and state-of-health of lithium-ion batteries," *Appl. Energy*, vol. 86, no. 9, pp. 1506–1511, Sep. 2009.

[3] T. F. Fuller, M. Doyle, and J. Newman, "Relaxation phenomena in LithiumIonInsertion cells," *J. Electrochem. Soc.*, vol. 141, no. 4, p. 982, Apr. 1994.

[4] M. Aykol et al., "Perspective—Combining physics and machine learning to predict battery lifetime," *J. Electrochemical Soc.*, vol. 168, no. 3, Mar. 2021, Art. no. 030525.

[5] G. Plett, *Battery Management Systems: Equivalent-Circuit Methods Volume II*, 2nd ed., Norwood, MA, USA: Artech House, Nov. 2015.

[6] J. Peng, J. Luo, H. He, and B. Lu, "An improved state of charge estimation method based on cubature Kalman filter for lithium-ion batteries," *Appl. Energy*, vol. 253, Nov. 2019, Art. no. 113520.

[7] M.-K. Tran et al., "A comprehensive equivalent circuit model for lithium-ion batteries, incorporating the effects of state of health, state of charge, and temperature on model parameters," *J. Energy Storage*, vol. 43, Nov. 2021, Art. no. 103252.

[8] Q. Yu, R. Xiong, C. Lin, W. Shen, and J. Deng, "Lithium-ion battery parameters and state-of-charge joint estimation based on H-infinity and unscented Kalman filters," *IEEE Trans. Veh. Technol.*, vol. 66, no. 10, pp. 8693–8701, Oct. 2017.

[9] H. Beelen, H. J. Bergveld, and M. C. F. Donkers, "Joint estimation of battery parameters and state of charge using an extended Kalman filter: A single-parameter tuning approach," *IEEE Trans. Control Syst. Technol.*, vol. 29, no. 3, pp. 1087–1101, May 2021.

[10] D. Carnevale, C. Possieri, and M. Sassano, "State-of-charge estimation for lead–acid batteries via embeddings and observers," *Control Eng. Pract.*, vol. 85, pp. 132–137, Apr. 2019.

[11] E. L. Haseltine and J. B. Rawlings, "Critical evaluation of extended Kalman filtering and moving-horizon estimation," *Ind. Eng. Chem. Res.*, vol. 44, no. 8, pp. 2451–2460, Apr. 2005.

[12] X. Hu, D. Cao, and B. Egardt, "Condition monitoring in advanced battery management systems: Moving horizon estimation using a reduced electrochemical model," *IEEE/ASME Trans. Mechatronics*, vol. 23, no. 1, pp. 167–178, Feb. 2018.

[13] J.-N. Shen, J.-J. Shen, Y.-J. He, and Z.-F. Ma, "Accurate state of charge estimation with model mismatch for Li-ion batteries: A joint moving horizon estimation approach," *IEEE Trans. Power Electron.*, vol. 34, no. 5, pp. 4329–4342, May 2019.

[14] P. Kühl, M. Diehl, T. Kraus, J. P. Schlöder, and H. G. Bock, "A real-time algorithm for moving horizon state and parameter estimation," *Comput. Chem. Eng.*, vol. 35, no. 1, pp. 71–83, Jan. 2011.

[15] E. D. R. Lopes, M. M. Soudre, C. H. Llanos, and H. V. H. Ayala, "Nonlinear receding-horizon filter approximation with neural networks for fast state of charge estimation of lithium-ion batteries," *J. Energy Storage*, vol. 68, Sep. 2023, Art. no. 107677.

[16] B. Wang, Z. Ma, S. Lai, and L. Zhao, "Neural moving horizon estimation for robust flight control," *IEEE Trans. Robot.*, vol. 40, pp. 639–659, 2024.

[17] C. Zou, C. Manzie, D. Nešić, and A. G. Kallapur, "Multi-time-scale observer design for state-of-charge and state-of-health of a lithium-ion battery," *J. Power Sources*, vol. 335, pp. 121–130, Dec. 2016.

[18] F. Oliva and D. Carnevale, "Moving horizon estimator with filtering and adaptive sampling," *IFAC-PapersOnLine*, vol. 55, no. 16, pp. 320–325, Jan. 2022.

[19] F. Oliva and D. Carnevale, "On the implementation of adaptive and filtered MHE," 2022, *arXiv:2204.09359*.

[20] T. Desai, F. Oliva, R. M. G. Ferrari, and D. Carnevale, "Real-time battery state of charge and parameters estimation through multi-rate moving horizon estimator," *IFAC-PapersOnLine*, vol. 56, no. 2, pp. 6124–6129, Oct. 2023.

[21] X. Hu, S. Li, and H. Peng, "A comparative study of equivalent circuit models for Li-ion batteries," *J. Power Sources*, vol. 198, pp. 359–367, Jan. 2012.

[22] H. Rahimi-Eichi, F. Baronti, and M.-Y. Chow, "Online adaptive parameter identification and state-of-charge coestimation for lithium-polymer battery cells," *IEEE Trans. Ind. Electron.*, vol. 61, no. 4, pp. 2053–2061, Apr. 2014.

[23] F. Zheng, Y. Xing, J. Jiang, B. Sun, J. Kim, and M. Pecht, "Influence of different open circuit voltage tests on state of charge online estimation for lithium-ion batteries," *Appl. Energy*, vol. 183, pp. 513–525, Dec. 2016.

[24] R. Tousain, E. van der Meche, and O. Bosgra, "Design strategy for iterative learning control based on optimal control," in *Proc. 40th IEEE Conf. Decis. Control*, Dec. 2001, pp. 4463–4468.

[25] A. Wynn, M. Vukov, and M. Diehl, "Convergence guarantees for moving horizon estimation based on the real-time iteration scheme," *IEEE Trans. Autom. Control*, vol. 59, no. 8, pp. 2215–2221, Aug. 2014.

[26] W. Kang, "Moving horizon numerical observers of nonlinear control systems," *IEEE Trans. Autom. Control*, vol. 51, no. 2, pp. 344–350, Feb. 2006.

[27] D. Aeyels, "On the number of samples necessary to achieve observability," *Syst. Control Lett.*, vol. 1, no. 2, pp. 92–94, Aug. 1981.

[28] J. C. Goswami and A. K. Chan, *Fundamentals of Wavelets: Theory, Algorithms, and Applications*. Hoboken, NJ, USA: Wiley, 2011.

[29] C. Torrence and G. P. Compo, "A practical guide to wavelet analysis," *Bull. Amer. Meteorological Soc.*, vol. 79, no. 1, pp. 61–78, Jan. 1998.

[30] (2015). *Battery Research Data*. Accessed: May 25, 2024. [Online]. Available: https://calce.umd.edu/data

[31] Y. Wang, H. Fang, L. Zhou, and T. Wada, "Revisiting the state-of-charge estimation for lithium-ion batteries: A methodical investigation of the extended Kalman filter approach," *IEEE Control Syst. Mag.*, vol. 37, no. 4, pp. 73–96, Aug. 2017.